



A multiscale simulation framework of the accumulative roll bonding process accounting for texture evolution



A. Prakash ^{a,*}, W.G. Nöhring ^{a,b,1}, R.A. Lebensohn ^c, H.W. Höppel ^a, E. Bitzek ^a

^a Department of Materials Science and Engineering, Institute I, Friedrich-Alexander-Universität Erlangen-Nürnberg (FAU), 91058 Erlangen, Germany

^b Elite Master's Programme in Advanced Materials and Processes (MAP), Friedrich-Alexander-Universität Erlangen-Nürnberg (FAU), 91058 Erlangen, Germany

^c Los Alamos National Laboratory, Los Alamos, NM 87545, USA

ARTICLE INFO

Article history:

Received 14 November 2014

Received in revised form

4 February 2015

Accepted 5 February 2015

Available online 13 February 2015

Keywords:

Accumulative roll bonding (ARB)

Visco plastic self-consistent (VPSC)

Multiple pass rolling

Solution variables mapping

Finite element (FE) multi-level

parallelization

Ultra-fine-grained (UFG) aluminum

ABSTRACT

The accumulative roll bonding process is one of the most prominent severe plastic deformation processes for obtaining sheet materials with ultra-fine-grained microstructures and high strength. The properties of such sheets differ significantly from those of conventionally rolled sheets. It is hence desirable to have a simulation framework that can accurately predict the material properties, including the evolving texture and anisotropy during processing. Here, we propose such a framework for *multiple pass* rolling using explicit finite elements and embedding the visco-plastic self-consistent (VPSC) polycrystal texture model for the material response. To facilitate multiple pass rolling, we propose a novel solution mapping scheme that transfers the material state from the deformed finite element mesh to a new one. Additionally, we implement a two-level parallelization scheme – with decomposition of the FE domain using message passing interface (MPI) and thread based parallelization of the material response using OPENMP – to ensure reduced simulation times. The predictive capabilities of the proposed framework are demonstrated by simulating the accumulative roll bonding of aluminum alloy AA5754 sheets. The simulations validate the working of the solution mapping scheme, and clearly show the development of a through thickness gradient of texture and anisotropy in the roll-bonded sheet after two passes.

© 2015 Elsevier B.V. All rights reserved.

1. Introduction

The adoption of new materials in the automotive, aerospace or energy sectors hinges ever increasingly on the possibility to reliably model their mechanical behavior during processing and under typical usage conditions, as well as their failure when subjected to catastrophic loading, e.g. during a car crash. Material models have therefore become an essential ingredient for the emerging discipline of *integrated computational materials engineering* (ICME), which promises to significantly shorten the materials development cycle [1]. For example, the integration of computational material models in the product design process as well as in manufacturing process simulation would allow engineers to explore new ways of optimizing the properties of a component through processing. The key for successful implementation of the ICME paradigm is the availability of material models which describe the multiple links among processing, microstructure,

properties and performance in a multiscale modeling framework. However, for many innovative materials or processing routes reliable material models are not yet available. In particular, the *accumulative roll bonding* process to produce high strength metal sheets, e.g. for automotive applications, would profit from a reliable and robust material model to optimize the process parameters and describe the resulting microstructure and mechanical properties.

Among the various *severe plastic deformation* (SPD) processes, the *accumulative roll bonding* (ARB) process is most promising for achieving ultra-fine-grained (UFG) microstructures in metallic sheet materials. First proposed by Saito et al. [2], the ARB process is based on the principle of stacking two sheets of materials and subsequently feeding them to a rolling mill where the thickness is reduced by 50%. As the geometrical dimensions of the processed sheet remain more or less unchanged to the starting material, the process can be easily repeated. Both sheets are initially degreased and wire brushed to remove thick oxide layers; in the absence of such oxide layers and driven by large plastic strains, the stacked layers fuse at the interface to ensue good bonding properties. A detailed overview on the principles of ARB-processing and the properties of some processed materials is provided in Ref. [3]. A

* Corresponding author.

E-mail address: arun.prakash@fau.de (A. Prakash).

¹ Currently at: Laboratory for Multiscale Mechanics Modeling, École Polytechnique Fédérale de Lausanne, CH-1015 Lausanne, Switzerland.

major advantage of the ARB process is that it can be easily integrated/adapted into existing industrial rolling trains without major modifications and can be scaled up to produce sheet materials with UFG microstructures on an industrial scale [4]. Furthermore, the ARB process offers numerous possibilities to tailor materials properties by producing laminated sheet materials [5–7], graded structures [8], particulate [9,10] or fiber reinforced composite sheet materials [11–13].

The repeated roll bonding of the sheets in the ARB process leads to substantial accumulation of plastic deformation resulting in a UFG microstructure. This UFG microstructure causes a significant increase—by almost a factor of two—in the strength of the material, in comparison to the coarse grained counterpart. Although this is generally offset by a decrease in ductility, it has recently been reported that application of ARB to low density sheet materials, like aluminum alloys, can result in both high strength and high ductility of the material [5] and has been attributed to room temperature strain rate sensitivity of the material (see also e.g. [14–16]).

The ARB process itself involves a multitude of parameters, e.g. rolling speed, friction between the rolls and the feedstock, number of rolling passes, and stacking and rolling direction, which can have a considerable effect on the properties of the roll bonded sheet. Although comparable to a conventional rolling process in principle, the role of such process parameters is either significantly enhanced or completely different in ARB due to the high thickness reduction and repeated stacking of roll bonded sheets in every pass. For instance, sheared surface layers (due to friction between the rolls and the feedstock) give rise to a characteristic through thickness strain gradient in the roll bonded sheet. With repeated cutting and stacking, the shear profile changes substantially [14], leading to different rates of microstructure evolution along the thickness of the sheet. Consequently, the number of rolling passes has a discernible effect on the through thickness strain gradient. The anisotropy in the roll bonded sheet is thus not just a function of texture/microstructure, but also the strain gradient and the number of rolling passes [17]. It is thus to be expected that the properties of ARB sheets differ appreciably from those of conventionally rolled sheets [18], and additionally, can significantly impact further applications (e.g. deep drawing) of the roll bonded sheet.

In view of the aforementioned aspects, it is desirable to have a computational framework to simulate and understand the ARB process in order to obtain optimized process parameters, so as to avoid trial-and-error experimental setups. To date, most studies on ARB processed materials have been experimental investigations to understand both the process and the enhanced properties of the roll bonded sheet, as evident in the references mentioned above. By contrast, few computational studies can be found in the literature; these studies have been limited to understanding individual aspects of the ARB process. For instance, texture evolution which plays an important role during ARB has been the subject of a few numerical investigations. Heason and Prangnell [19] performed EBSD and X-ray measurements on a roll bonded AA1100 sheet, and analyzed the evolution of texture using the Taylor [20] full constraints model with simple and idealized textures. A similar study was performed on AA3003 by Pircgazi et al. [21], but by using the ALAMEL model [22]. In contrast to the idealized deformation paths assumed in the previous two studies, Li et al. [23] used realistic strain histories to investigate the texture evolution in commercially pure aluminum by means of the ALAMEL model. Finite element (FE) simulations of a *single-pass* rolling process were employed to obtain the relevant strain histories; the FE simulations were calibrated to embedded pin experiments in order to reasonably estimate the shear deformation [24] seen in ARB processed materials.

A primary goal of this work is to establish a computational framework that enables the simulation of *multiple pass* ARB process, while simultaneously accounting for the change in texture and anisotropy of the material. The principal idea here is to obtain the structural response using a FE calculation, while the material response is obtained by “averaging” the constitutive behavior of individual crystals in a defined polycrystal. Such “averaging”, termed generally as *numerical homogenization*, is now a well established technique to solve problems involving the micro-mechanical behavior of polycrystalline materials. An excellent review of such methods is provided in Ref. [25]. Although different flavors of such a multi-scale framework are available, all boil down essentially to two choices: (a) the polycrystal homogenization theory to be used [26], i.e. *full-field* or *mean-field* theory, and (b) implementation of the mesoscopic model within the multi-scale analysis framework [22], i.e. whether the polycrystal model is to be *embedded* in the FE computation, or merely used in a *hierarchical* fashion.

Polycrystal homogenization theories can be broadly classified into two categories, viz. full-field and mean-field methods. Full-field methods provide a fairly accurate assessment of the intragranular stress and strain fields. Examples of such methods include the *crystal plasticity finite element method* (CPFEM) and *crystal plasticity fast Fourier transform* (CPFFT) method. CPFEM has been extensively used with artificial microstructures (e.g. [27–29]) as well as experimental microstructures obtained typically from EBSD measurements (e.g. [30–32]). The CPFFT method [33,34] is identical to CPFEM with one major difference – the governing equations are solved in the Fourier space. Although restricted to periodic microstructures in principle, a major advantage of CPFFT over CPFEM is the speed of computation [35]. The choice of such full field methods for numerical homogenization, however, necessitates the usage of FE^2 -type methods (e.g. [36]), which would essentially result in lengthy computation times for multiple pass ARB simulations.

In what concerns the implementation of the numerical homogenization model within the multiscale analysis framework [22], choice must be made between *embedding* the model in the FE computation—i.e. interrogating the polycrystal model during each increment—and using it in a *hierarchical* fashion [37,38], where the parameters for a macro-scale (anisotropic) phenomenological yield criterion (e.g. [39,40]) are pre-computed by interrogating the polycrystal model. This choice, as a result, is clearly a decision on balancing accuracy and speed, since embedded models tend to be more accurate but less efficient (in terms of computational times) than hierarchical models. Nonetheless, it must be noted that adaptive sampling strategies (e.g. [41]) can be used in conjunction with embedded models to achieve results in shorter lead times.

The fundamentals of our computational framework lie in the aforementioned multiscale approach; we use a mean field homogenization model *embedded* in a FE computation. In particular, we use the viscoplastic self-consistent (VPSC) model of Lebensohn and Tomé [42] as our choice of the mean field model, since it has been widely used for many studies involving both cubic (e.g. [43]) and *hcp* (e.g. [44–46]) materials and is known to provide fairly accurate predictions of the texture and anisotropy [47,48]. The VPSC model is embedded in an explicit finite element framework using the commercial finite element software ABAQUS. It must be pointed out that this embedded VPSC-FE model is not entirely new, and has been the subject of previous studies (e.g. [44,49,50]). However, such basic implementations are insufficient to overcome the challenges posed by the ARB process.

A primary challenge in simulating the ARB process – as seen from the discussion before – is the increase in number of elements, by a factor of two, with each ARB pass. Additionally, due to the

large thickness reduction in each rolling pass, distortion of the FE mesh is a further problem that needs to be tackled. In view of this, we propose a novel solution mapping scheme that helps map the texture, grain shape and other relevant material state variables from the deformed mesh to a new mesh, thus alleviating the distortion related problems. Also, since the mapping can be done to a completely new mesh, it allows us to circumvent the doubling of elements with each pass. Furthermore, we strive to create an implementation that is robust, fast and efficient. This is done by exploiting the vectorized interface of the user material routine in ABAQUS® by using a multi-level parallelization, i.e. decomposition of the FE domain for the structural response, and parallelization of the material response inside each domain using multiple OPENMP [51] threads. Additionally, we probe the polycrystal model only periodically, thus ensuring further improvement in simulation times. We point out that notwithstanding the results presented in the current work, the proposed computational framework can be used for the simulation of other forming processes like conventional rolling and deep drawing.

The paper is organized as follows: following this introductory section, we first present the constitutive framework used in this work in Section 2, and subsequently its implementation as a user material in Section 3. Results of ARB simulations are presented in Section 4, wherein the working of the novel solution mapping scheme is also demonstrated. The significance of the results is discussed in Section 5. Finally, we conclude by providing a summary of our results in Section 6.

2. Constitutive framework

2.1. Viscoplastic self-consistent formulation

The viscoplastic self-consistent (VPSC) model of Leibsohn and Tomé [42] used in the current work, is a homogenization model that treats each grain in a polycrystalline aggregate as an equivalent inclusion in a fully anisotropic visco-plastic matrix, also referred to as the homogeneous equivalent medium (HEM). The compatibility between the inclusion and matrix is enforced using the *Eshelby inclusion formalism* [52]. In what follows, certain key equations of the VPSC model are presented for completeness and to facilitate easy understanding of the symbols/parameters used in the model and its implementation as a user material routine for finite elements.

Within the setting of the VPSC model, a polycrystal is modeled as a set of discrete weighted orientations of ellipsoidal shape. Each discrete orientation represents the average behavior of all grains with the crystallographic orientation under consideration, but embedded in different environments.

The constitutive response of a single crystal is assumed to be rigid viscoplastic, with plasticity occurring as a consequence of glide systems becoming active. Each system is defined by a glide direction, \mathbf{s} , and a normal to the glide plane, \mathbf{n} . The geometry of the slip system is described by the symmetric \mathbf{m}^α and antisymmetric β^α parts of the Schmid tensor:

$$\begin{aligned}\mathbf{m}^\alpha &= \frac{1}{2}(\mathbf{s}^\alpha \otimes \mathbf{n}^\alpha + \mathbf{n}^\alpha \otimes \mathbf{s}^\alpha) \\ \beta^\alpha &= \frac{1}{2}(\mathbf{s}^\alpha \otimes \mathbf{n}^\alpha - \mathbf{n}^\alpha \otimes \mathbf{s}^\alpha),\end{aligned}\quad (1)$$

where \otimes denotes the diadic product of two vectors. The shear rate on any glide system is given by the following rate-sensitive equation:

$$\dot{\gamma}^\alpha = \dot{\gamma}_0 \left(\frac{|\tau^\alpha|}{g^\alpha} \right)^n \times \text{sign}(\tau^\alpha) \\ = \dot{\gamma}_0 \left(\frac{|\mathbf{m}^\alpha : \boldsymbol{\sigma}'|}{g^\alpha} \right)^n \times \text{sign}(\mathbf{m}^\alpha : \boldsymbol{\sigma}'),\quad (2)$$

where τ^α is the resolved shear stress on the glide plane under consideration, g^α is the current strength of the glide system, $\dot{\gamma}_0$ is a reference shear rate, n is the rate sensitivity exponent and $\boldsymbol{\sigma}'$ denotes the deviatoric Cauchy stress tensor. The overall viscoplastic strain rate of the crystal is given by the sum of individual crystallographic shear rates [53,54]

$$\begin{aligned}\dot{\epsilon}^p(\mathbf{x}) &= \sum_{\alpha=1}^{N_s} \mathbf{m}^\alpha(\mathbf{x}) \dot{\gamma}^\alpha(\mathbf{x}) \\ &= \dot{\gamma}_0 \sum_{\alpha=1}^{N_s} \mathbf{m}^\alpha \left(\frac{\mathbf{m}^\alpha : \boldsymbol{\sigma}'}{g^\alpha} \right)^n \times \text{sign}(\mathbf{m}^\alpha : \boldsymbol{\sigma}'),\end{aligned}\quad (3)$$

where N_s denotes the number of active slip systems. Eq. (3) may be rewritten in the pseudo-linear form

$$\begin{aligned}\dot{\epsilon}^p &= \left\{ \dot{\gamma}_0 \sum_{\alpha=1}^{N_s} \frac{\mathbf{m}^\alpha \otimes \mathbf{m}^\alpha}{g^\alpha} \left(\frac{\mathbf{m}^\alpha : \boldsymbol{\sigma}'}{g^\alpha} \right)^{n-1} \right\} \boldsymbol{\sigma}' \\ &= \mathbb{M}^{c(sec)}(\boldsymbol{\sigma}') : \boldsymbol{\sigma}',\end{aligned}\quad (4)$$

where $\mathbb{M}^{c(sec)}$ denotes the so-called secant viscoplastic compliance tensor of the grain. Another relation may be derived using a Taylor expansion:

$$\dot{\epsilon}^p = \dot{\epsilon}_0^p + \left. \frac{\partial \dot{\epsilon}^p}{\partial \boldsymbol{\sigma}'} \right|_{\boldsymbol{\sigma}'=\bar{\boldsymbol{\sigma}}} \boldsymbol{\sigma}' = \mathbb{M}^{c(tg)}(\bar{\boldsymbol{\sigma}}') : \boldsymbol{\sigma}' + \dot{\epsilon}_0^p,\quad (5)$$

which defines the tangent modulus $\mathbb{M}^{c(tg)}$ and the back extrapolated term $\dot{\epsilon}_0^p$. From Eqs. (3)–(5), it follows that

$$\mathbb{M}^{c(tg)} = n \mathbb{M}^{c(sec)}. \quad (6)$$

We assume that the overall response of the polycrystal is described by constitutive equations similar to those of the single crystal (Eqs. (4) and (5)). The secant relation of the polycrystal is given by

$$\dot{\mathbf{E}}^p = \mathbb{M}^{(sec)}(\Sigma') : \Sigma', \quad (7)$$

where $\dot{\mathbf{E}}^p$ and Σ' are the strain rate and deviatoric stress, respectively, of the polycrystal. The tangent relation, valid only in the vicinity of $(\bar{\Sigma}')$ adopts the form

$$\dot{\mathbf{E}}^p = \mathbb{M}^{(tg)}(\bar{\Sigma}') : \Sigma' + \dot{\mathbf{E}}_0^p. \quad (8)$$

The polycrystal tangent and secant moduli are related by the same relation derived earlier for the single crystal moduli [55]

$$\mathbb{M}^{(tg)} = n \mathbb{M}^{(sec)}. \quad (9)$$

Each grain in the polycrystal can be regarded as an *ellipsoidal* inhomogeneity embedded in the HEM that induces *eigenstrains* locally upon the application of a remote stress to the HEM. The link between strain rates and stresses in the polycrystal and individual grains is now established using the notion of an *equivalent inclusion* [52,56]. In this context, the inhomogeneity (grain) is replaced by an equivalent inclusion having the same moduli as that of the HEM, but undergoing a fictitious transformation strain rate $\dot{\epsilon}^*$ that induces the same stress in the inclusion and in the HEM, as the inhomogeneity does. Hence Eq. (5) can be re-written as

$$\dot{\epsilon}^p = \mathbb{M}^{(tg)} : \boldsymbol{\sigma}' + \dot{\mathbf{E}}_0^p + \dot{\epsilon}^*, \quad (10)$$

within the domain of the inclusion. The deviations in the stress and strain rate fields in the inclusion with respect to the polycrystal are given by

$$\begin{aligned}\tilde{\epsilon}^p &= \dot{\epsilon}^p - \dot{\mathbf{E}}^p \\ \tilde{\boldsymbol{\sigma}'} &= \boldsymbol{\sigma}' - \Sigma'.\end{aligned}\quad (11)$$

Inserting Eq. (11) in Eq. (10) with Eq. (8) one obtains

$$\tilde{\epsilon} - \dot{\epsilon}^* = \mathbb{M}^{(tg)} : \tilde{\boldsymbol{\sigma}}'. \quad (12)$$

The strain rate deviation in the inclusion is given by

$$\tilde{\epsilon}^p = \mathbb{S} : \dot{\epsilon}^*, \quad (13)$$

where \mathbb{S} , the symmetric viscoplastic Eshelby tensor, is a function of the polycrystal tangent modulus and the grain shape, assumed to be ellipsoidal in the VPSC model. Therefore, an accurate description of the interaction between HEM and the grains (governed by \mathbb{S}), and consequently the state and response of the polycrystal, requires deft handling of the grain shape evolution. This is of particular importance when the state of the polycrystal is transferred from one finite element mesh to another, as is the case in the rolling simulations presented in this work. Aspects related to the handling of grain shape evolution are provided subsequently in Section 2.2.2.

Let us now introduce the interaction equation, which is obtained by replacing Eq. (13) in Eq. (12),

$$\tilde{\epsilon}^p = -\tilde{\mathbb{M}} : \sigma'. \quad (14)$$

This interaction equation formally links the fluctuations in stress and strain. The interaction tensor $\tilde{\mathbb{M}}$ defined by

$$\tilde{\mathbb{M}} = (\mathbb{I} - \mathbb{S})^{-1} \cdot \mathbb{S} \cdot \mathbb{M}^{(tg)}, \quad (15)$$

where \mathbb{I} is the fourth-order identity tensor.

What remains now is the evaluation of the viscoplastic moduli of the HEM, which are not known a priori. The assumption that the HEM describes the average behavior of the aggregate leads to the condition that the weighted average of stress and strain rate over all the grains must be equal to the stress and strain rates of the HEM. This condition enforces the self-consistent nature of VPSC and provides an expression from which the secant modulus of the HEM and the interaction tensor can be calculated. Eq. (14) can be reformulated using Eqs. (4) and (7) as follows:

$$\mathbb{B}^c : \Sigma' = \sigma', \quad (16)$$

where

$$\mathbb{B}^c = (\mathbb{M}^{(sec)} + \tilde{\mathbb{M}})^{-1} \cdot (\mathbb{M}^{(sec)} + \tilde{\mathbb{M}}), \quad (17)$$

defines the so-called accommodation tensor. The secant relation Eq. (4) for the grain is now given by

$$(\mathbb{M}^{(sec)} \cdot \mathbb{B}^c) : \Sigma' = \dot{\epsilon}^p. \quad (18)$$

Since the weighted average of the strain rate must be equal to the strain rate of the HEM,

$$\langle \mathbb{M}^{(sec)} \cdot \mathbb{B}^c \rangle : \Sigma' = \mathbb{M}^{(sec)} : \Sigma'. \quad (19)$$

Eq. (19) is fulfilled when

$$\mathbb{M}^{(sec)} = \langle \mathbb{M}^{(sec)} \cdot \mathbb{B}^c \rangle. \quad (20)$$

With $\mathbb{M}^{(sec)}$ given by the fix-point Eq. (20), the interaction tensor can be obtained as

$$\tilde{\mathbb{M}} = n(\mathbb{I} - \mathbb{S})^{-1} : \mathbb{S} : \mathbb{M}^{(sec)}. \quad (21)$$

The above expression corresponds to the original *tangent* formulation of [57] and [42], and has the disadvantage of going to the lower-bound (uniform-stress) in the rate sensitive limit ($n \rightarrow \infty$). The so-called *n-effective* variant of VPSC model [58] avoids this by using a correction factor n^{eff}/n in the interaction tensor, which yields

$$\tilde{\mathbb{M}} = n^{eff}(\mathbb{I} - \mathbb{S})^{-1} : \mathbb{S} : \mathbb{M}^{(sec)}. \quad (22)$$

The typical value $n^{eff} = 10$ has been used in all cases that follow.

2.2. Evolution of microstructure

2.2.1. Texture

Upon convergence in the iterative procedure to compute the state of the polycrystal, each grain is reoriented before proceeding to the next deformation step. The reorientation is described by the rate of spin and is given by [59]

$$\dot{\omega} = \dot{\Omega} + (\mathbb{W} \cdot \mathbb{S}^{-1}) : \tilde{\epsilon} - \omega^p, \quad (23)$$

where \mathbb{W} denotes the rotational (skew-symmetric) Eshelby tensor. ω^p is the antisymmetric part of the plastic distortion rate, $\dot{\Omega}$ is the antisymmetric component of the macroscopic distortion rate which can be obtained by the classical additive decomposition of the velocity gradient \mathbf{L}

$$\mathbf{L} = \mathbf{D} + \dot{\Omega}, \quad (24)$$

and $\dot{\omega}^p$ is the antisymmetric component of the plastic distortion rate given by

$$\dot{\omega}^p = \sum_{\alpha} \beta^{\alpha} \dot{\gamma}^{\alpha}. \quad (25)$$

It must be pointed out that reorientation of grains can also occur due to twinning, which is also a feature of the VPSC model. However, deformation due to twinning is not a part of the current work, and is hence not discussed here. Nevertheless, we emphasize that the simulation framework provided in this work is not restricted to dislocation plasticity alone, and can be used for materials which evidence significant twinning activity.

2.2.2. Grain shape

As mentioned earlier, the Eshelby tensor \mathbb{S} defines the solution of the equivalent inclusion problem, and is a function of the polycrystal tangent moduli $\mathbb{M}^{(tg)}$ and the grain shape. The evolution of the average grain shape is calculated using the polycrystal's velocity gradient \mathbf{L} defined in Eq. (24) and an average deformation gradient tensor \mathbf{F} that characterizes the average shape of the grains, which is initially assumed to be the identity tensor, thus representing equiaxed grains before the ARB process. The rate of variation of \mathbf{F} and the velocity gradient \mathbf{L} are related by

$$\dot{\mathbf{F}} = \mathbf{LF}. \quad (26)$$

Hence, knowing \mathbf{F} at time t , its value at time $t + \Delta t$ is obtained as

$$\mathbf{F}|_{t+\Delta t} = (\mathbb{I} + \mathbf{L} \Delta t) \mathbf{F}|_t. \quad (27)$$

The eigenvectors and the square root of the eigenvalues of \mathbf{FF}^T define the direction and length of the axes of the ellipsoid which represents the average shape of the grains.

2.2.3. Hardening

The evolution of the critical stress in Eq. (2) is determined by an extended Voce-type hardening rule [60,61]

$$\dot{g}^{\alpha} = \frac{d\bar{g}^{\alpha}}{d\Gamma} \sum_{\beta} h^{\alpha\beta} \dot{\gamma}^{\beta}, \quad (28)$$

with the hardening function

$$\bar{g}^{\alpha} = \tau_0^{\alpha} + (\tau_1^{\alpha} + \theta_1^{\alpha} \Gamma) \left[1 - \exp \left(-\frac{\theta_0^{\alpha} \Gamma}{\tau_1^{\alpha}} \right) \right], \quad (29)$$

where $h^{\alpha\beta}$ is a hardening matrix whose diagonal elements denote self-hardening and off-diagonal elements denote latent hardening. The cumulative shear, Γ , in the grain is defined as

$$\Gamma = \int_0^t \sum_{\alpha} \dot{\gamma}^{\alpha} dt. \quad (30)$$

3. Implementation as a user material subroutine

The commercial finite element software ABAQUS® is used in this work for the simulation of the ARB process. In particular, we use the explicit version of the software since it has been reported to perform well under complex loading conditions, including contact [62]. Furthermore, ABAQUS/Explicit allows for a more efficient domain decomposition and scales better with an increasing number of domains in the simulation. Consequently, larger and more complex geometries can be discretized with a fine mesh, making it an appropriate tool for the analysis of metal forming simulations.

An enterprising feature of ABAQUS/Explicit is the vectorized interface of the user material subroutine (VUMAT), where the constitutive update is expected for a block of integration points. This facilitates a thread based parallelization of the user material subroutine using OPENMP, and is described in more detail in subsequent sections. Since a considerable portion of the simulation dwells on the constitutive update, such a thread based parallelization should lead to a significant reduction in computation times, and is evident in the results presented later in this work.

At this juncture, it is worth reviewing previous implementations of the VPSC model into finite element codes. Tomé et al. [48] formulated the VPSC model as a user material for the explicit finite element code EPIC, and applied it to analyze the mechanical behavior of zirconium [45]. The first implementation in the finite element software ABAQUS was by Walde and Riedel [63] who later applied it to study the earing behavior in magnesium alloy AZ31 [44], and anisotropy in molybdenum sheets [64]. More recently, Segurado et al. [49] proposed the implementation of the VPSC model in the framework of *implicit* finite elements as a UMAT, which was later extended to include dislocation density based hardening to model the anisotropic response of α -uranium [50]. Incidentally, these implementations fail to exploit the vectorized interface of the VUMAT.

In what follows, we first review certain fundamental aspects of ABAQUS/Explicit in general, and the VUMAT in particular, by summarizing key equations [65]. Subsequently, we provide details on the VUMAT interface for VPSC and the linear updating scheme. Finally aspects related to parallelization of the VUMAT are dealt with.

3.1. VPSC–VUMAT interface

As with any embedded polycrystal model, each integration point in our FE mesh is assumed to be comprised of a polycrystal whose mechanical response is provided by the VPSC model. The VUMAT is called in a given time step for each integration point; it provides the strain increment along with the current state of the material. The user material routine is expected to provide the updated material state, which consists of both stresses and internal variables that describe the state of the polycrystal.

The constitutive update is required to be performed using the Green–Nagdhi objective stress rate [65], which is defined as

$$\dot{\sigma} = \dot{\sigma} - \Omega \cdot \sigma + \sigma \cdot \Omega, \quad (31)$$

where Ω denotes the rate of spin and can be calculated using the rotation tensor R obtained from the polar decomposition of the deformation gradient F as follows:

$$\Omega = \dot{R} \cdot R^T. \quad (32)$$

All input variables in the VUMAT are provided in a corotational system defined by the Green–Nagdhi objective stress rate.

The strain increment ($\Delta\epsilon$) provided by the VUMAT is assumed to undergo an additive decomposition, into an elastic ($\Delta\epsilon^e$) and an inelastic/viscoplastic ($\Delta\epsilon^p$) part:

$$\Delta\epsilon = \Delta\epsilon^e + \Delta\epsilon^p = C^{-1} : \Delta\sigma + \Delta\epsilon^p, \quad (33)$$

where C is the elastic stiffness of the polycrystal defined at any integration point and $\Delta\sigma$ is the increment of the Cauchy stress. In this work, we calculate C using an elastic self-consistent estimate (cf. Eq. (20)) as

$$C = \langle C^{c-1} : B^c \rangle^{-1}, \quad (34)$$

where C^c and B^c are the elastic stiffness and the stress localization tensors of individual grains. Such an approach effectively decouples the elastic and viscoplastic self-consistent responses, as suggested in Ref. [66], and must be deemed as a simplification of more involved elasto-viscoplastic self-consistent approaches (e.g. [67]).

The constitutive update of the stresses at any integration point can now be written as follows:

$$\sigma|_{(t+\Delta t)} = \sigma|_t + C : (\Delta\epsilon - \Delta\epsilon^p). \quad (35)$$

If $\Delta\epsilon^p$ were to be known, it could be used to interrogate the VPSC model to obtain the homogenized visco-plastic response of the underlying polycrystal at a FE material point for the imposed boundary conditions. However, since $\Delta\epsilon^p$ is not known a priori, we use a stress driven algorithm to interrogate the VPSC model.

The algorithmic structure of the stress driven approach to interrogate VPSC is derived from Segurado et al. [49], and can be seen as an alternative to the approach of Walde and Riedel [44]. We proceed by defining a residual χ as an implicit function of the current stress increment such that

$$\begin{aligned} \chi &= \Delta\epsilon - \Delta\epsilon^{FE} \\ &= C^{-1} : \Delta\sigma + \Delta t \dot{E}^p(\sigma + \Delta\sigma) - \Delta\epsilon^{FE}, \end{aligned} \quad (36)$$

where $\Delta\epsilon^{FE}$ is the total strain increment provided by ABAQUS in the VUMAT. The residual equation is minimized using the Newton–Raphson procedure to obtain a new iterative stress state:

$${}^{k+1}\Delta\sigma = {}^k\Delta\sigma - J_{NR}^{-1}({}^k\Delta\sigma) : \chi({}^k\Delta\sigma), \quad (37)$$

where the left superscript denotes the iteration. The Jacobian is defined by

$$\begin{aligned} J_{NR} &= \frac{\partial \chi(\Delta\sigma)}{\partial(\Delta\sigma)} \\ &= C^{-1} + \Delta t \frac{\partial \dot{E}^p}{\partial(\Delta\sigma)} \\ &= C^{-1} + \Delta t M^{tg}(\sigma + \Delta\sigma), \end{aligned} \quad (38)$$

where M^{tg} represents the polycrystal tangent moduli. Upon convergence, the current stress increment is returned to the FE solver. The algorithmic structure has the advantage that the update of stresses follows an implicit time integration scheme. Nonetheless, the update of other internal variables related to hardening, texture and morphology is updated explicitly. Due to the usage of a very small time increment in ABAQUS/Explicit, such an explicit update of internal variables is not expected to lead to major discrepancies.

3.2. Piecewise linear stress update

The conditional stability of the ABAQUS/Explicit solver necessitates the usage of a very small time increment, leading to a very high number of total time steps in the simulation. The VPSC constitutive update, however, becomes no less simplified with the usage of the small time increment. In fact, since the stress update is a function of the polycrystal moduli (M^{tg}), which itself needs to

be obtained iteratively, a straightforward implementation of VPSC as an embedded constitutive model would result in exorbitantly high computation times. Furthermore, since $\mathbb{M}^{(tg)}$ involves the inversion of crystal moduli $\mathbb{M}^{(tg)}$ which is a function of the resolved shear stresses, a small initial time step from a stress free state would result in individual components of the crystal moduli $\mathbb{M}^{(tg)}$ being close to zero resulting in an ill-conditioned matrix for inversion.

To overcome these problems, we use a piecewise linear updating scheme which circumvents the VPSC call if certain criteria are met. This linear stress update is defined by the following equation:

$$\Delta\sigma = \mathbb{C} : (\Delta\epsilon^{FE} - \dot{\mathbf{E}}^p \Delta t) \quad (39)$$

where \mathbb{C} denotes the polycrystal elastic moduli obtained from the elastic self-consistent calculation and $\dot{\mathbf{E}}^p$ denotes the plastic strain rate of the polycrystal computed in the last VPSC call.

A two step criterion is employed to check if a linear update has to be performed. At the beginning of each increment, we calculate the ratio between the von Mises equivalent stress (σ_{vm}) and the initial maximum critical resolved shear stress ($g_{0,max}^\alpha$):

$$s_{norm} = \frac{\sigma_{vm}}{g_{0,max}^\alpha}. \quad (40)$$

A linear update is enforced if this ratio is below a certain threshold s_{norm}^{thres} . If the condition is not satisfied, i.e. $s_{norm} > s_{norm}^{thres}$, then two further quantities, viz. the accumulated equivalent stress ($\Delta\sigma_{acc,vm}^{thres}$) and strain ($\Delta\epsilon_{acc,vm}^{thres}$) since the last VPSC update, are evaluated. If either of these two quantities, however, violate a particular threshold, then a VPSC update is enforced. **Table 1** lists the numerical values of the thresholds used in the current work, which have been chosen to best represent the material behavior under consideration.

We note that grain shapes, orientations and hardening variables are not updated when a linear stress update is performed. When the VUMAT decides to call VPSC, the values of the relevant variables accumulated since the last VPSC call are provided as input to the VPSC model. In effect, the evolution of the viscoplastic polycrystal state is equivalent to a simulation with a larger time increment but purely VPSC constitutive update.

3.3. Parallelization

In the VUMAT, the FE solver requests the constitutive response for a *block* of integration points. Since the constitutive update of an individual integration point is independent of any neighboring integration points, one can envisage a loop based parallelization using OPENMP [51]. Such a parallelization is independent of, and/or in addition to, decomposition of the finite element domain into subdomains – also referred to as domain decomposition based parallelization. The resultant simulation scheme is hence essentially a *multi-level* parallelized framework; the structural response is obtained by *domain decomposition of the FE mesh using message passing interface (MPI)* and the material response is obtained by *decomposing the constitutive update onto multiple cpus using OPENMP threads*.

Table 1
Thresholds for the piecewise linear updating scheme.

Parameter	Threshold
s_{norm}^{thres}	0.5
$\Delta\sigma_{acc,vm}^{thres}$	15 MPa
$\Delta\epsilon_{acc,vm}^{thres}$	0.001

Such a parallelization is, however, not completely straightforward. Care must be taken to ensure proper load balancing so that both highly strained and unstrained regions are equally distributed among all processors. A dynamic schedule of the OPENMP *parallel* loop over the block of integration points is hence preferred over a completely static schedule because of the load imbalance that is likely to occur during the simulation of the ARB process; elements directly under the roller would essentially require frequent calls to VPSC as against those far away from the roller.

3.4. Solution mapping of the polycrystal state

In order to facilitate the simulation of a multiple pass ARB process, we propose a novel method to map the solution dependent variables from the deformed mesh to a new mesh before the subsequent pass. The procedure, in brief, works as follows. The polycrystal material state at each integration point is saved at the end of each rolling pass. The material state so obtained is then mapped onto a new mesh by interpolating between the material states of adjacent integration points.

The mapping procedure allows the user to use a FE mesh of good quality for each pass, thus alleviating mesh deterioration problems due to the high thickness reduction (50%) in each pass. Furthermore, using the mapping procedure we can circumvent the doubling of elements due to stacking of sheets before each pass; in the limiting case, a constant number of elements can be used for each pass. Thus the amount of book keeping necessary to store and manipulate the underlying polycrystal state of the finite element mesh can be kept to a minimum.

A primary requirement for any mapping of the finite element solution from one mesh to another must be the equivalency of the material state, i.e. the mapped material state must deliver the same mechanical response as that of the original mesh. To this extent, we first need to identify the variables in VPSC (and VUMAT) that define the state of the polycrystal. **Table 2** lists the variables that need to be used in the mapping procedure. We motivate these variables from the secant/tangent viscoplastic compliance of a crystal, which in essence defines the state of the grain. Upon investigation of Eq. (4), it is clear that the secant moduli is a function of the grain orientation, making it a primary variable to be accounted for in the mapping procedure. Since the stress in a grain is accounted for by the critical resolved shear stresses, we affix g^α also to the solution mapping set. The evolution of the critical resolved shear stresses depends on the cumulative shear Γ in the grain, making it the third variable in the solution mapping set. Note that Γ also defines the strain state of the grain. Finally, we note that the evaluation of the Eshelby tensor, which is required for computing the response of the *equivalent inclusion*, is a function of the grain shape. Consequently, we append the deformation gradient \mathbf{F}^c that defines the grain shape to the set.

We now take a look into the mapping procedure itself, which is inherently a linear interpolation scheme. We note that the variables summarized in **Table 2** are primarily of two types – scalars and tensors. The linear interpolation of scalars (in this work, cumulative shear and the critical resolved shear stresses of each

Table 2
Set of variables for the solution mapping procedure.

Description	Symbol	Type
Cumulative shear	Γ	Scalar
Critical resolved shear stress	g^α	Scalar
Grain deformation gradient	\mathbf{F}^c	Tensor
Grain orientation	\mathbf{g}^c	Tensor

grain) is straightforward and is not discussed here. Among the tensorial variables, we first consider the grain orientation which is represented using Euler angles in the VPSC code. Direct interpolation/mapping of Euler angles, however, leads to spurious rotations [68]. Consequently, we interpolate the grain orientation in the quaternion representation using the spherical linear interpolation (SLERP) algorithm [69] as follows:

$$\mathbf{q}_{int} = \frac{\sin((1-\bar{x}_{int})\Theta)}{\sin\Theta}\mathbf{q}_a + \frac{\sin(\bar{x}_{int}\Theta)}{\sin\Theta}\mathbf{q}_b, \quad (41)$$

with

$$\cos\Theta = \mathbf{q}_a \cdot \mathbf{q}_b, \quad (42)$$

where \mathbf{q}_a and \mathbf{q}_b are the quaternions corresponding to an orientation at the reference points, \mathbf{q}_{int} denotes the quaternion representing the orientation at the interpolated point, and Θ is the angle of the arc between \mathbf{q}_a and \mathbf{q}_b on the unit sphere in four-dimensional space. \bar{x}_{int} is a number between 0 and 1, and is the relative position of the interpolation point with respect to the reference points:

$$\bar{x}_{int} = \frac{x_{int} - x_a}{x_b - x_a}. \quad (43)$$

Direct transformation rules for converting quaternions to Euler angles and vice versa are not provided here for the sake of brevity. For more details on the same, the reader is referred to standard literature on the subject, e.g. [70].

Finally we take a look into the mapping of the shape tensor \mathbf{F}^c , which is basically the deformation gradient tensor of the grain under consideration. Direct interpolation of the deformation gradient tensor can result in artificial distortions. To avoid these spurious effects, we exploit the polar decomposition of the deformation gradient as follows:

$$\mathbf{F}^c = \mathbf{R}^c \cdot \mathbf{U}^c, \quad (44)$$

where \mathbf{U}^c and \mathbf{R}^c represent the right stretch tensor and the rotation tensor, respectively, of the crystal. The rotation tensors of the reference points are transformed into quaternions and then mapped onto the new point using the SLERP algorithm (Eq. (42)). The stretch tensors, on the other hand, are interpolated linearly onto the new point.

In view of the amount of book-keeping necessary for the storage of individual grain shapes, and in order to ensure simulations in reasonable time frames, we use only the average grain shape of the polycrystal for the interpolation. The mapping procedure described above is, however, a general framework that can also be used on individual grains in the polycrystal.

4. ARB simulations

The accumulative roll bonding process was simulated using the OPENMP parallelized VPSC VUMAT in combination with the linear elastic update described in Section 3.2. The working of the VUMAT was first verified by performing benchmark tests on a single element and loading it in uniaxial tension, uniaxial compression and simple shear. Comparison of the results with those from the standalone version (ver.7) of the VPSC code [71] showed identical stress strain responses and textures, indicating the correctness of the VUMAT implementation. Further tests with multiple elements were performed to ensure the sanity of the parallelized code. These results of these benchmark tests are provided elsewhere [72,73].

The simulations shown here consist of two rolling passes. To model stacking of sheets before the second pass, the required internal variables were mapped onto a new mesh using the procedure described in Section 3.4.

4.1. Simulation setup

The FE model used for the ARB simulations is shown in Fig. 1. The model is set up such that the rolling, transverse and normal directions are parallel to the x -, y - and z -axis, respectively. The feedstock consists of two Al5754 sheets, of length 5 mm and thickness 1 mm, stacked upon each other. The Voce hardening parameters for the material are taken from Ref. [74]. Symmetry conditions are exploited by modeling only one half of the feedstock (i.e. only one of the two Al5754 sheets) in the simulations. The above condition has the consequence that bonding between the two sheets is essentially modeled as “hard” contact, with debonding of the rolled sheets precluded. The modeled sheet is discretized with 500 hexahedral elements; reduced integration elements (C3D8R) with enhanced stiffness hourglass control are used in the simulations.

In addition to symmetry, plane strain conditions are imposed in the transverse direction, resulting effectively, in the simulation of a thin slab of material in the center of a fairly wide sheet, as shown in Fig. 1(b). Such a model provides a more accurate material response – for which it is primarily set up, and allows additionally for a relatively fine spatial discretization.

The rollers, modeled as rigid with a diameter of 32 mm, rotate at a speed of 80 rpm. Contact between the roller and the feedstock is imposed through an isotropic friction coefficient of $\mu = 0.4$. Mass scaling is used to artificially increase the stable time increment, while taking care to keep the kinetic effects of such a scaling to a minimum. The used stable time increment in the simulations is $\Delta t = 4 \times 10^{-6}$ s. The simulations are carried out in parallel with eight OPENMP threads, but without domain decomposition.

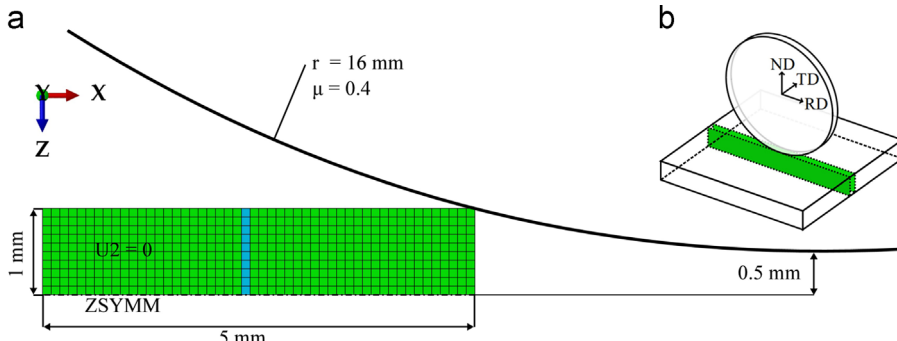


Fig. 1. Initial configuration used for simulations of the ARB process. The blue strip indicates the elements for which texture and polycrystal states are saved. (For interpretation of the references to color in this figure caption, the reader is referred to the web version of this paper.)

For the first rolling pass, all elements in the feedstock are initialized with identical texture comprising 250 spherical grains of random orientation and equal volumes. Texture output, along with additional internal variables (cf. Table 2) are requested as so-called *end-of-pass data* for 10 elements along the cross Section of the feedstock (marked in blue in Fig. 1). These elements have been purposefully chosen along the center of feedstock, so as to avoid boundary effects likely to be present around the ends of the roll bonded sheet.

For the second rolling pass, the same finite element model is retained. However, the modeled feedstock is now assumed to be a roll bonded sheet obtained from the first rolling pass. To effectively carry over the material state from the first rolling pass to the second, we use the solution mapping procedure described previously in Section 3.4. To this end, we use the material state of the ten elements marked in blue in Fig. 1.

The mapping is done as follows. Since the original thickness of the sheet is 1 mm, and the thickness reduction imposed in the first pass is 50%, the z-coordinate (normal direction) of the centroid of all the ten elements (forming the top sheet in the first pass) may be expected to lie between 0 mm and 0.5 mm. Now five evenly spaced points at 0.05, 0.15, 0.25, 0.35 and 0.45 mm are selected in this interval. If a neighborhood is now established based purely on the z-coordinate, each new element may be considered to be in the vicinity of two polycrystal states of the roll bonded sheet. A new state is then generated for each of the five points by linearly interpolating the two neighbor polycrystal states. This mapping procedure is schematically represented in Fig. 2.

We note that each vertical *slab* of 10 elements in the new FE mesh corresponds effectively to 20 polycrystal states (or stacking of two sheets) in the ARB sheet obtained after the first pass. The five newly generated polycrystal states are copied onto the lower set of 5 elements, assuming a mirror symmetric stacking sequence. The state of the polycrystal in this vertical stack of 10 elements is now replicated along the length of the sheet. In effect, we have now mapped the material state of the deformed FE mesh of the first pass to the undistorted initial mesh of the second pass.

It must be pointed out that the usage of only 10 polycrystal states for the mapping procedure is a matter of convenience. A more elaborate schema could be envisaged, wherein the *end-of-pass* data of all elements in the deformed finite element mesh could be used for the mapping procedure, thus resulting in an

improved representation of the microstructural inhomogeneity. The usage of such an extensive set would, however, necessitate data throughput between individual computation processes and physical memory storage leading to significant increase in simulation times.

With the polycrystal states accounted for, the second rolling pass can be simulated in a straightforward manner like the first pass. The same process parameters as that of the first pass are retained for the simulation of the second pass.

4.2. Results

Fig. 3 shows the distribution of von Mises equivalent stresses in the deformed geometry after the first and second rolling pass. Towards either end of the rolled sheet, the deformation is clearly inhomogeneous. However, for a greater part of the sheet around the center, a steady stress distribution is observed. It is exactly in this region that we request the texture and *end-of-pass* data, in order to obtain a material state that is by and large reflective of the rolled sheet. The ten elements, numbered between 261 and 270, from which the material state is used for the mapping procedure are also indicated in Fig. 3.

The textures obtained from the aforementioned central stack of elements after the first ARB pass is shown in Fig. 4. The pole figures were computed using the Matlab toolbox MTEX [75]. A clear gradient in the texture is evident through the thickness of the sheet. The elements towards the center of the sheet exhibit a texture close to typical rolling textures of face centered cubic (*fcc*) materials, while those towards the surface of the sheet evidence an additional shear component. This can be better understood by looking at Fig. 5(a) which shows the components of textures in individual elements. Towards the center of the sheet, the texture is dominated by the *S* and *Brass* components, along with considerable contributions of the *Copper* and *Taylor* components indicating a strong *fcc* rolling texture. With increasing distance from the center, the relative volume fraction of these components decreases, while that of the rotated cube component increases reflecting a texture with significant shear deformation. This dominance of the rotated cube component at the surface of the sheet is noteworthy, particularly due to its relative absence at the center of the sheet.

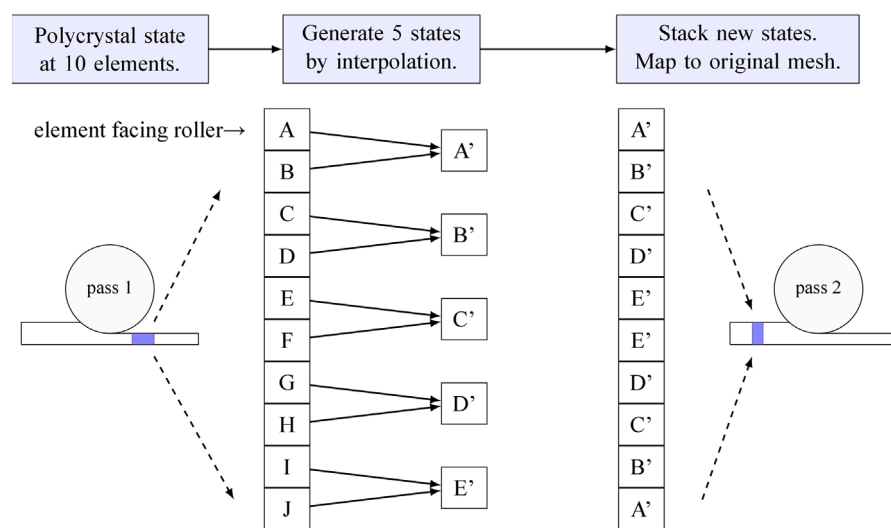


Fig. 2. A schematic of the solution mapping scheme that maps the polycrystal state after the first pass onto a new initial mesh for the second pass. Polycrystal states of ten elements marked in blue are mapped onto five elements by interpolating the states of adjacent elements. The mapped solution state is then duplicated in five more elements by assuming reflection symmetry. This new stack of ten elements with the mapped solution states is then replicated along the length of the FE mesh used for the subsequent pass. (For interpretation of the references to color in this figure caption, the reader is referred to the web version of this paper.)

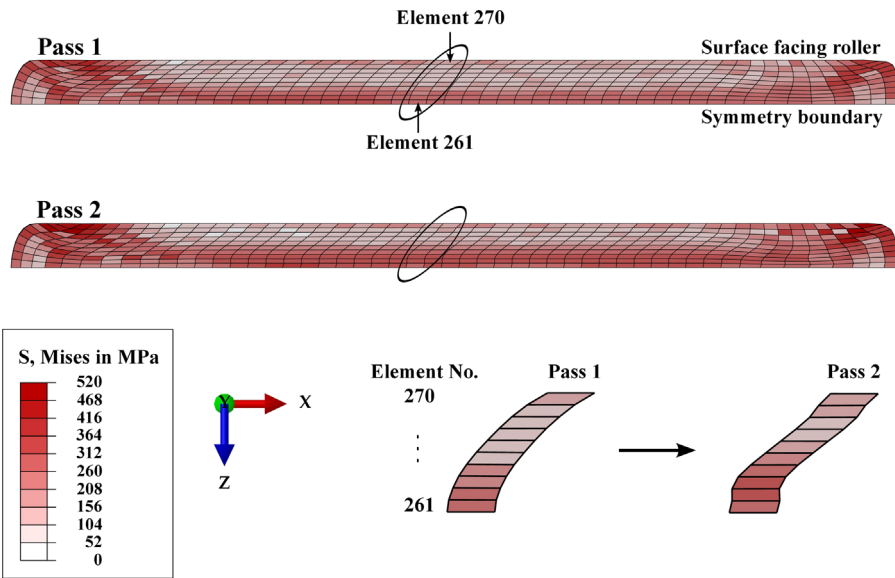


Fig. 3. Stress distribution (von Mises equivalent stress) in the rolled sheet after the first and the second pass. A steady distribution can be appreciated in greater part of the sheet, in which for a stack of ten elements the texture and end-of-pass data are requested as output. The close-up view shows the deformed shape of elements from which output has been requested. In both rolling passes, a through-thickness shear gradient can be clearly observed.

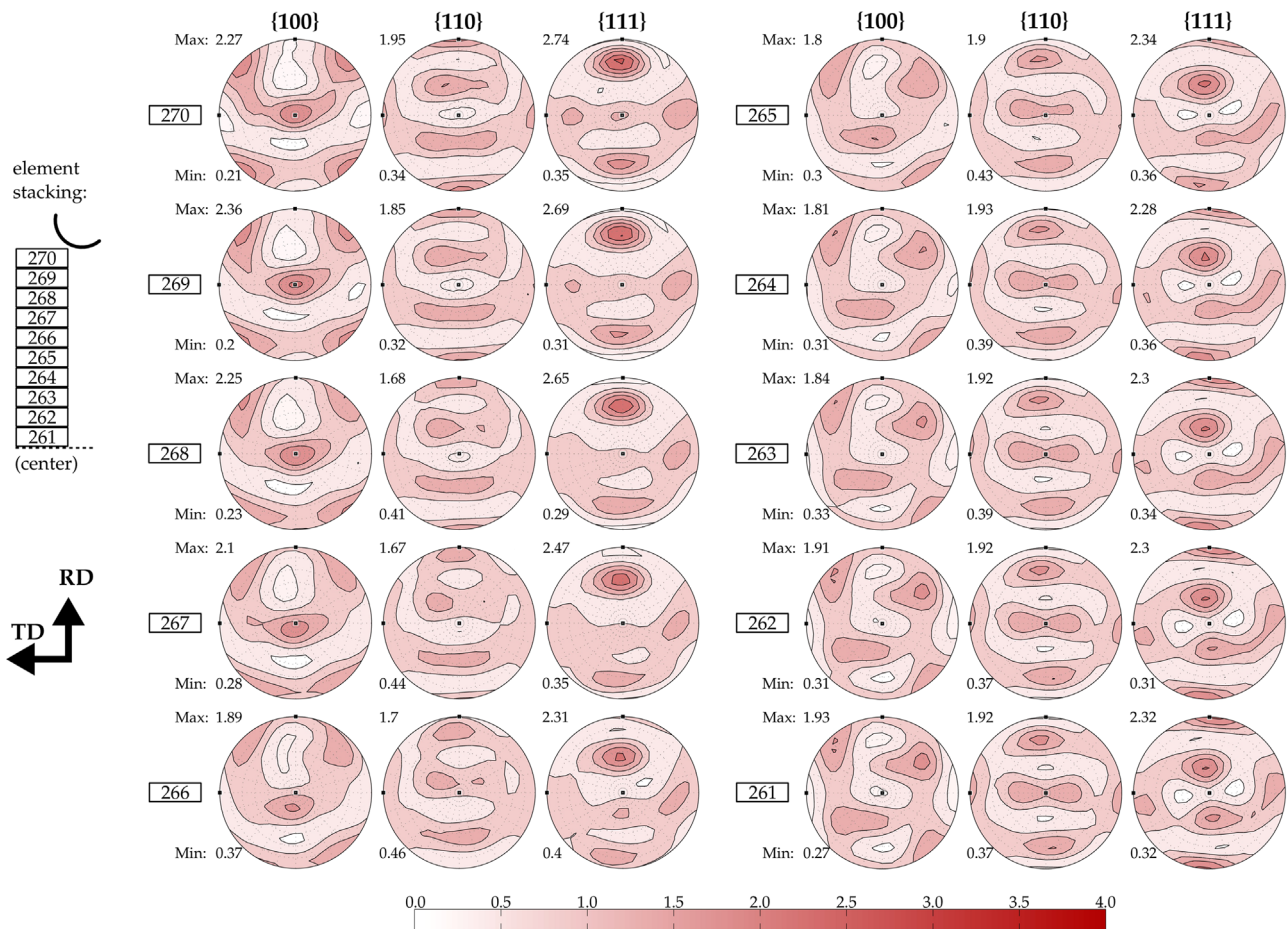


Fig. 4. Textures in the central stack of ten elements (cf. Fig. 1) after rolling pass 1. A through-thickness gradient in texture is evident. Near the sheet surface, the rotated cube component is dominant. Towards the center of the sheet stack, the texture shows typical rolling components.

The textures of this central stack of ten elements are then mapped onto the top five elements of the new mesh using the mapping procedure described previously in detail. The mapped textures are presented in Fig. 6. Essentially, the textures of two

adjacent elements (e.g. 270 and 269, or 268 and 267 in Fig. 6) in the thickness of the rolled sheet are then mapped onto a single element (cf. A or B in Fig. 6) in the new mesh. Similitude between the mapped textures and the corresponding reference states can

be easily appreciated. Indeed the mapped texture, along with additional mapped variables that govern the state produce a mechanical response that lies between those of the reference

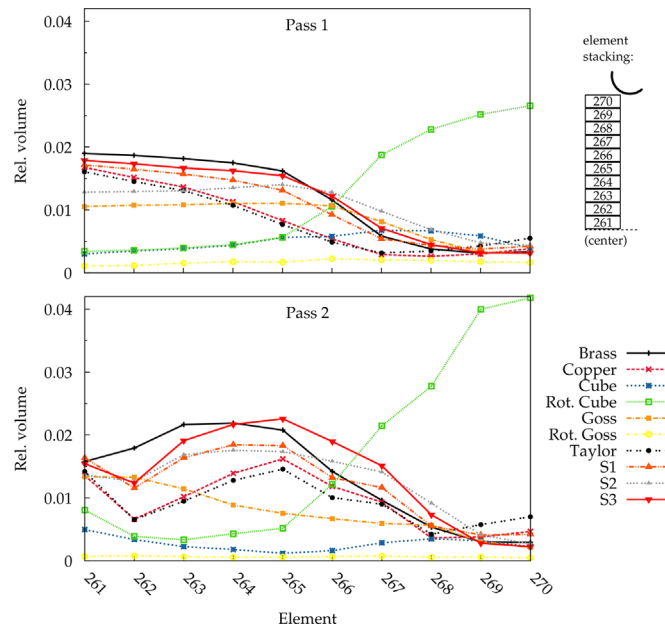


Fig. 5. Texture components in the central stack of ten elements (cf. Fig. 1) after the first and second rolling pass.

states. The initial state of the bottom five elements in the new mesh is then obtained by copying the state of the top five elements, albeit by reflection, so as to obtain a stacking sequence *Roller-A-B-C-D-E-E-D-C-B-A*. Consequently, the top sheet of the feedstock for ARB pass 2 has a shear dominated texture at its surface and a strong rolling texture at its center.

In addition to the textures, other variables defining the state of the polycrystal are also mapped onto the top five elements of the new mesh and copied onto the bottom five to obtain the stacking sequence as mentioned above. Of the remaining three solution variables (cf. Table 2), the mapping of critical resolved shear stresses and the cumulative shear, which are scalars, is straightforward and is not presented here for the sake of brevity. Mapping of the grain shapes, by contrast, is non-trivial and demands careful scrutiny. Fig. 7 shows the results of the grain shape mapping. The average shape of the polycrystal is initially a sphere and evolves into ellipsoids of varying shapes and orientations in each of the central stack of ten elements. For demonstration, the ellipsoids of four elements (numbered 261, 261, 269 and 270, and corresponding to two adjacent elements near the center and surface of the top sheet) after the first pass are shown in Fig. 7 (red ellipsoids). The mapped ellipsoids, shown in green, share a strong resemblance to the reference states in terms of not just the shape, but also the orientation. This clearly indicates the soundness of the mapping procedure. The mapped ellipsoids are then used as the initial average shape of the polycrystal for the second rolling pass. For completeness, the final shape of the two ellipsoids after the second pass is also shown in Fig. 7.

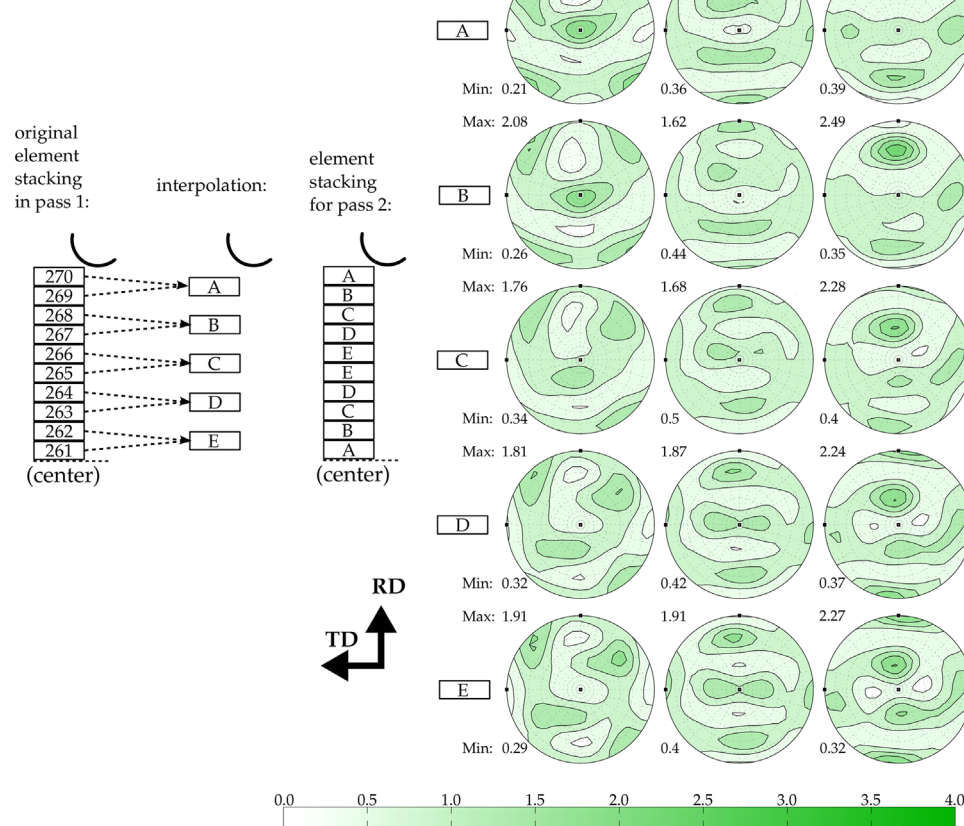


Fig. 6. Mapped textures, which serve as input for pass 2. Also shown is a schematic of the mapping between the reference stack of ten elements (numbered) and the top five elements in a stack of ten elements in the new mesh, which are then copied onto the bottom five elements through reflection. Similitude between the mapped textures and the corresponding reference states from pass 1 (Fig. 4) is evident.

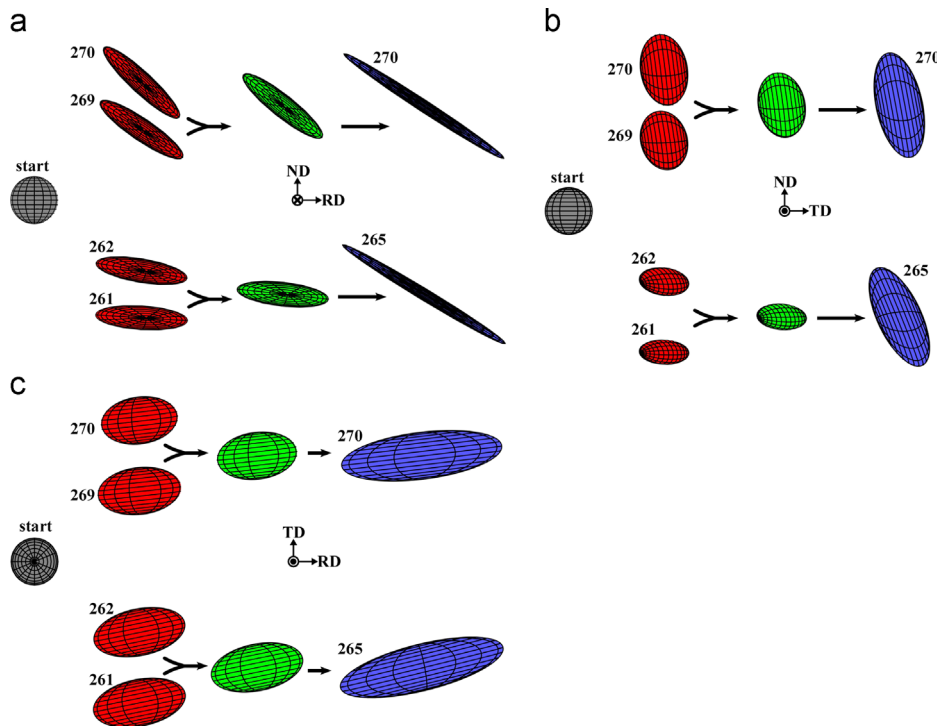


Fig. 7. Front (a), side (b) and top (c) views of the average ellipsoids used in the ARB simulations. Gray: common initial grain shape; red: grain shape in elements 261, 262, 269 and 270 after the first rolling cycle; green: interpolated grain shapes for starting configuration of elements 265 and 270 in the second rolling pass. The interpolated shape of 265 is based on the shape in element 261 and 262; for the interpolated shape in 270 the reference states are 269 and 270. Blue: shape in elements 265 and 270 after the second cycle. (For interpretation of the references to color in this figure caption, the reader is referred to the web version of this paper.)

We note that for the second pass, further simulation parameters from the first pass are retained. Symmetry boundary conditions are once again exploited to reduce the size of the simulated domain. This inevitably leads to rolling of two sheets, where the properties of the bottom sheet are mirror symmetric to those of the top sheet. For the current scenario, where the process involves roll bonding of two sheets of the same material, this does not make a difference. However, for the simulation of roll bonding of laminates, symmetry boundary conditions must be used with caution.

The textures after the second rolling pass are presented in Fig. 8, with the volume fractions of different texture components plotted in Fig. 5(b). The output is again requested in the central stack of elements, as in the first pass. Similar to the first pass, elements close to the sheet surface show a texture with considerable amount of shear, characterized by a strong rotated cube component. A reduction in the volume fraction of the rotated cube component towards the center of the rolled sheet is simultaneously followed by an increase in the volume fraction of the S and Brass components. However, in contrast to the first pass where a gradual increase of the S-component towards the center of the sheet was seen, a peak around apparently the center of top sheet is seen. We ascribe this to the presence of a strong rolling texture at the center of the roll bonded sheet after the first pass.

The gradient observed in the texture of the rolled sheet has considerable influence on the yield behavior of the sheet. Fig. 9 shows the polycrystal yield surfaces of the central stack of ten elements for which output of the material state was requested. The yield surfaces are projected onto the σ_{11} – σ_{22} plane, assuming plane stress conditions ($\sigma_{33} = 0$). In addition to the yield surfaces after the first and second rolling passes, we also present the initial yield surface (polycrystal with 250 randomly oriented grains) for comparison. The yield surfaces after the first and second rolling passes have been calculated with standalone VPSC by using the texture and *end-of-pass* polycrystal states of the central stack of ten elements as input.

The yield surface of the initial configuration is more or less isotropic, and its shape can be approximately characterized by the von Mises yield criterion. As expected, with each rolling pass, isotropic hardening leads to an increase in the size of the yield surface, with a higher hardening rate in the first pass than in the second. Noticeably, this isotropic hardening leads to almost no change in the shape of the yield surface in the element close to the center of the rolled sheet and is evidently a consequence of the underlying strong rolling texture. The domination of shear in the elements close to the surface leads to an anisotropic evolution of the shape of the yield surface, and the shape can no longer be characterized by a simple von Mises type of yield criterion. A more detailed discussion on the shape of the yield surfaces is presented in Section 5.

4.3. Simulations with a 3D model

A further important aspect of the current work is the usage of multi-level parallelization – domain decomposition using MPI and parallelization of the VUMAT using OPENMP. To address this issue, we performed full three dimensional simulations of the ARB process, using different parallelization combinations and a moderately fine mesh. The initial and deformed FE models are shown in Fig. 10. It is clear from the stress distribution shown in Fig. 10b that the stress levels reached in the full 3D model are comparable to those in the plane strain rolling simulations, vindicating the plausibility of the quasi-2D approach presented in Section 4. However, more interesting are the computation times required for these full 3D computations. A simulation with *purely domain decomposition* based parallelization that uses 8 domains takes approximately 105 h. By contrast, a simulation using the *two level parallelization, with 2 domains and 4 threads* each takes merely 36 h. Note that in both these simulations the number of cpus used is essentially the same.

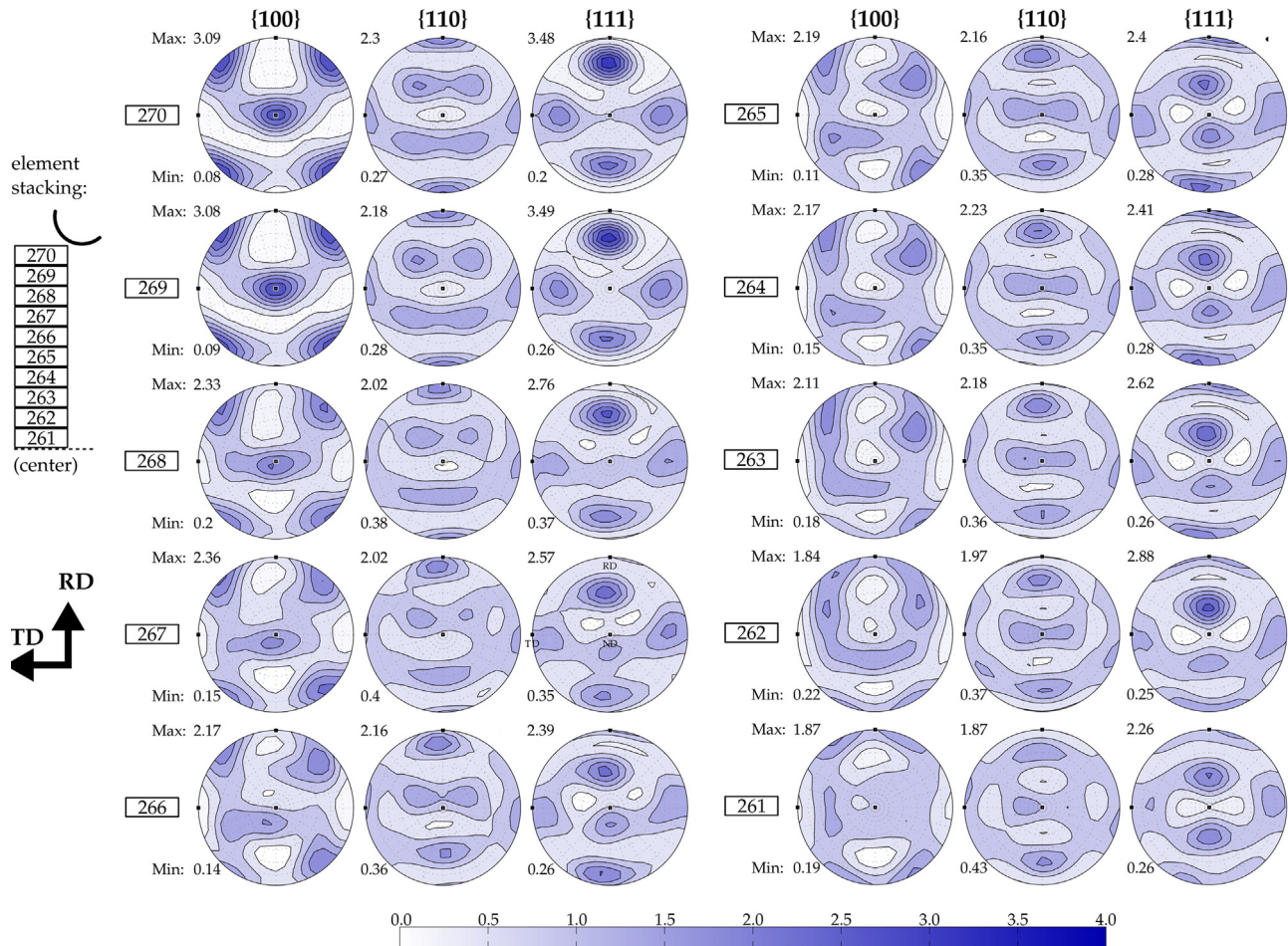


Fig. 8. Textures in the central stack of ten elements (cf. Fig. 1) after rolling pass 2. A through-thickness texture gradient is evident. The rotated cube component is dominant near the sheet surface. Rolling components are formed near the center of the sheet stack (see also Fig. 5).

These simulation times unambiguously show the potential for the novel computational framework proposed in the current work. The true advantage of the two level parallelization is indeed visible in simulations with larger domains where sufficient amount of work can be parallelized using OPENMP threads. The OPENMP based parallelization has the advantage of improved mitigation of load imbalance that might occur during the simulation of complex processes like ARB.

Nonetheless, it must be pointed out that load imbalance is still likely to be a problem due to the linear update of the constitutive response used in the current work. Recall that this is necessitated by the small stable time increment in ABAQUS/Explicit. Consequently, an embedded framework that calls the VPSC model in every increment becomes computationally exorbitant with increasing complexity of the FE model. Segurado et al. [49] show that the calculation of the consistent tangent moduli for *implicit* finite elements requires the mere addition of the elastic moduli (C) to the polycrystal tangent moduli (M) obtained from VPSC, necessitating the usage of acceleration techniques that call the embedded model only when required. The linear constitutive update is an example of such a technique and can easily lead to load imbalance in the OPENMP threads, but can be overcome by the usage of dynamic scheduling of the computation performed by each thread.

5. Discussion

The results of the ARB simulations show the formation of a texture gradient in the thickness of the sheet, after both rolling

passes. Although no experimental investigations were performed in the current work, the simulation results are seemingly consistent with experimental results of ARB processed aluminum alloys available in the literature. Saito et al. [2] identify a surface shear texture and a rolling texture in the bulk of an AA1100 sheets after eight ARB cycles. A texture gradient has also been observed in AA1100 (6 ARB cycles) [76] and in AA1070 (1,2,4 and 6 ARB cycles) [77]. Indeed, the formation of such a texture gradient is not exclusive to ARB processed alloys, and can be seen in conventional rolling processes too, albeit to a lesser degree.

A primary reason for this gradient is the difference in the imposed boundary conditions between elements on the surface of the rolled sheet and those at the center. The friction conditions between the roller and the feedstock results in a substantial amount of shear deformation in the elements close to the surface. This superposed shear deformation gradually reduces towards the center of the rolled sheet, a consequence of which, elements close to the center are subjected to almost pure plane strain compression boundary conditions. This is evident in both the predicted texture (cf. Figs. 4 and 5) and the deformed mesh of rolled sheet, as seen in Fig. 11 for a central stack of ten elements.

Since the ARB process involves stacking of two sheets before each pass, the central region of the feedstock (consisting of two sheets) before the second pass now essentially presents a shear texture. After the second pass, this shear texture is reduced considerably. Nevertheless, a gradient in texture is still evident, although the center of the top sheet still shows a strong fcc rolling texture.

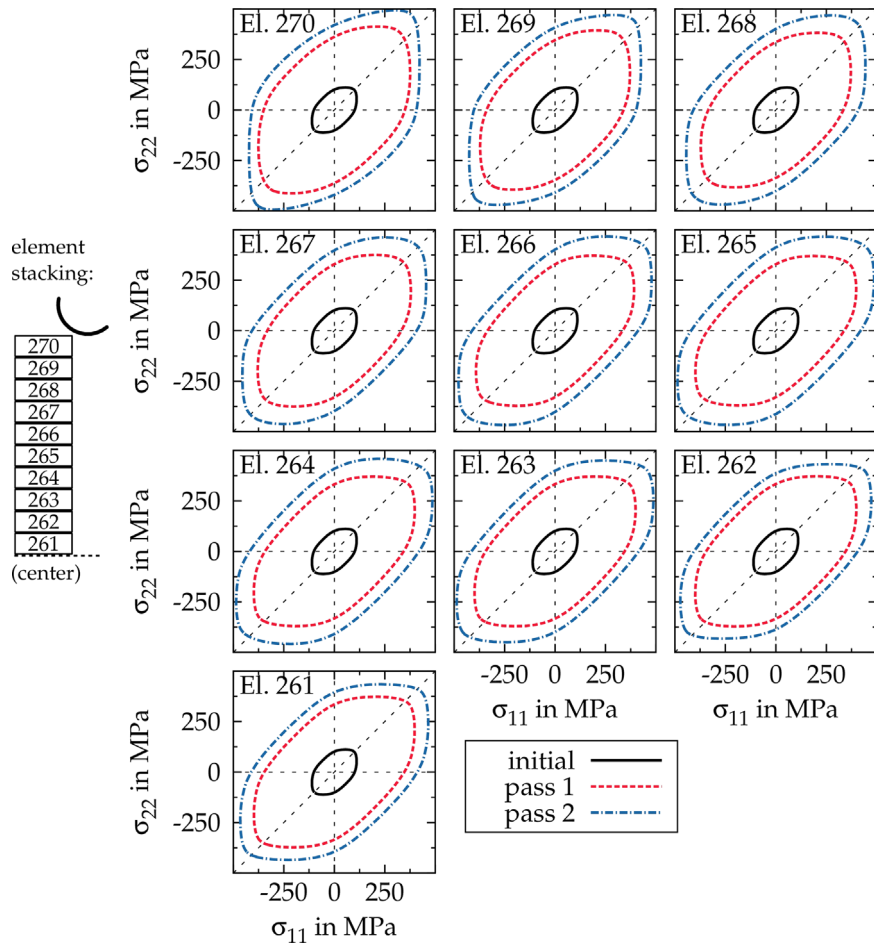


Fig. 9. Polycrystalline yield surfaces in initial state and after ARB pass 1 and 2. Towards the center of the sheet stack and especially in element 261, the yield surface undergoes a more or less isotropic evolution. At the sheet surface, in element 270, anisotropic evolution is observed.

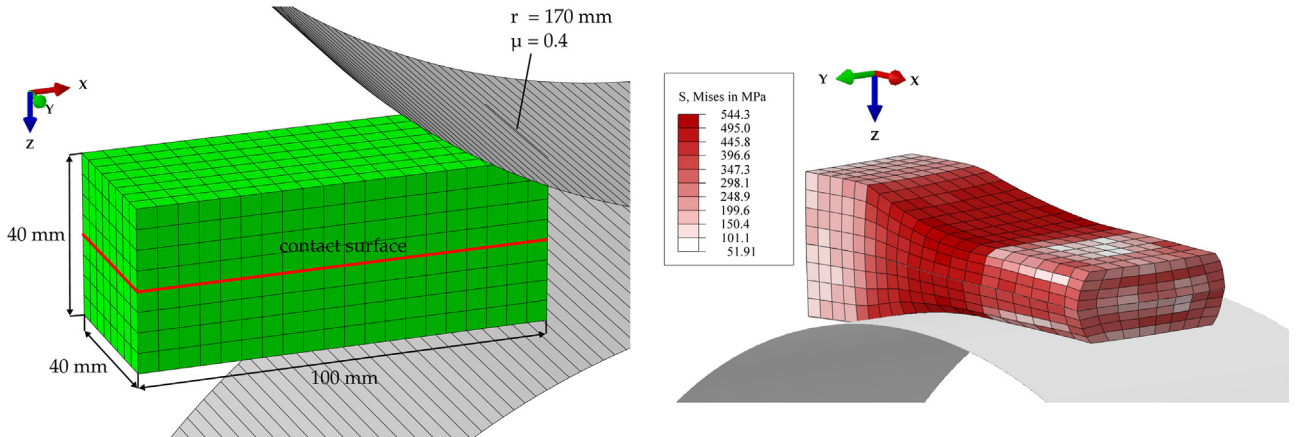


Fig. 10. Initial (left) and deformed (right) FE models of the full 3D simulations of the ARB process. The deformed structure shows the von Mises stress state in the material. A simulation with purely domain decomposition based parallelization that uses 8 domains takes approximately 105 h. By contrast, a simulation using the two level parallelization, with 2 domains and four threads each takes merely 36 h.

A direct consequence of the texture gradient in the thickness of the sheet is the differential evolution of the yield surfaces, as seen in Fig. 9. We take a closer look into the yield surfaces of two elements, one corresponding to the surface, and the other corresponding to the center of the ARB sheet. Fig. 12 shows the yield surfaces in these two elements after the second pass. For comparison, the yield contours of the classical Tresca [78] and von Mises [79] criteria are also plotted. The yield surfaces have been normalized using σ_{11} , in order to facilitate the comparison of shapes of the

yield surfaces. The initial random texture of both elements results effectively in a yield locus that is close to the von Mises criterion. At the end of the second pass, however, there is a discernible difference between the yield surfaces of the two elements. The yield locus of the surface element is highly anisotropic which can be attributed to the shear (accumulated with increasing number of passes) caused by the friction between the roller and the sheet. In comparison, the yield surface of the element close to the center evolves with lesser amount of anisotropy. Although the two

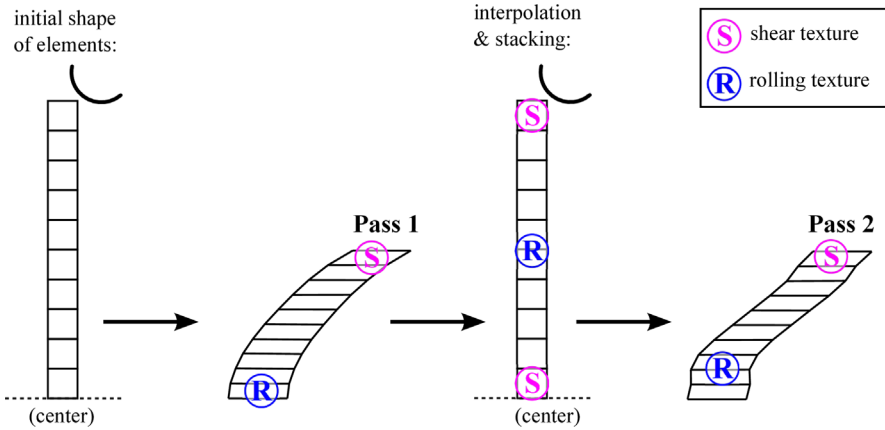


Fig. 11. Initial and deformed shapes of the elements in the center cross-section (marked blue in Fig. 1) for ARB pass 1 and 2, and locations where shear or rolling texture components are most pronounced. After the rolling pass, texture components are redistributed due to stacking of sheets. This results in a different through-thickness variation of shear in pass 2.

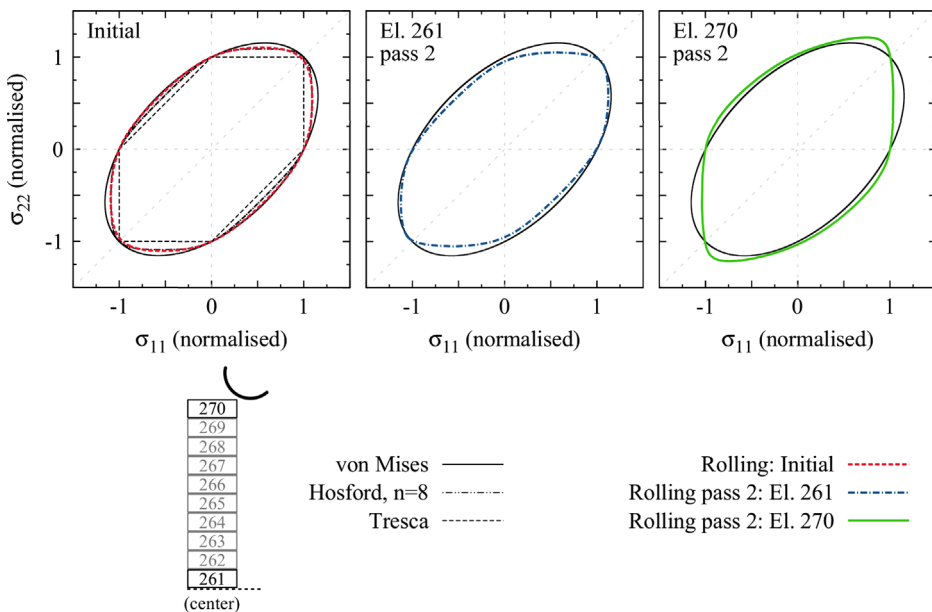


Fig. 12. Normalized polycrystalline yield surfaces of the initial state and in elements 261 and 270 after pass 2. The isotropic yield stresses according to the criteria of Tresca [78] and von Mises [79] are also included. Comparison shows that the yield stress is anisotropic after ARB pass 2. The anisotropy is more pronounced in case of the surface element 270.

elements in question experience the same amount of shear in the first pass, the element in the center experiences reduced or almost no shear in the second pass, and is dominated by boundary conditions close to plane strain compression.

This differential yield behavior is of significance for two additional reasons. First, this behavior is different from what can be expected in multiple pass direct rolling simulations. Or in other words, *the anisotropic evolution of the yield surfaces is a direct consequence of the stacking of sheets in the ARB process*. Second, engineers aiming to simulate further processes like deep drawing to determine component behavior and reliability must account for this through thickness gradient of the material properties; neglecting it may result in the incorrect estimation of the stress and strain state in the simulations.

The proposed modeling framework successfully captures key elements of the ARB process, namely rolling process along with the large thickness reduction, and the evolving texture and anisotropy. It also circumvents mesh deterioration problems in multiple pass rolling. However, in the present form, the framework does not yet include two further important aspects of the ARB process – interlayer

bonding strength and the refinement of grain size leading to UFG microstructure after multiple rolling passes. The modeling framework can, however, be easily extended to include additional features, like e.g. cohesive zone elements, to account for interlayer bonding.

The VPSC model embedded in the current framework uses a phenomenological description of the strain rate. This is clearly not sufficient to account for the complex deformation mechanisms and their temperature and strain rate dependence, which is of particular importance in UFG materials. A more physics based constitutive description is hence necessary to capture intricate details of the mechanics at the small length scales, including activation barriers [80], dislocation-defect interactions [81,82], grain boundary mediated plasticity [83–85], amongst others. These are aspects of current development involving physics based constitutive models (e.g. [86–88], see Ref. [25] for a detailed review on such models). The VPSC model can be directly extended to include such physics based constitutive approaches [89]. Likewise, constitutive models for grain refinement (e.g. [90]) can also be easily incorporated in the current framework to account for the UFG microstructure.

Even with its current limitations, the present multiscale modelling framework is expected to significantly contribute to the establishment of the ARB process as an elegant way to produce metal sheets with tailored properties. The framework can, for instance, be used to optimize processing parameters and conditions required for ARB. Having a reliable and robust simulation framework, which is simultaneously efficient so as to provide results in realistic time schedules, can help in *upscale*ing the process to produce sheets of large dimensions required for industrial usage. Furthermore, it can also be used for subsequent forming processes like deep drawing, thereby enabling the simulation of a process chain.

6. Conclusions

In this work, we have developed a computational framework that facilitates the simulation of multiple pass ARB process. To this end, we embed the VPSC model as a VUMAT in the explicit FE formulation of ABAQUS. As a result the evolution of texture during the process, and consequently the evolving anisotropy is seamlessly accounted for in the framework, and have a direct influence on the processing conditions, like e.g. rolling forces.

The main aspects of our framework are as follows:

- To facilitate the simulation of multiple passes, we propose and implement a novel *solution mapping* scheme. This scheme essentially maps the texture, grain shapes and other relevant material state variables from the deformed mesh onto a new undistorted mesh. As a result, simulation of the subsequent pass can be done with a mesh of good quality while retaining the requisite solution variables of the previous pass. This has an additional advantage of circumventing the problem associated with an increase in number of finite elements with increasing number of ARB passes, since the number of elements remains constant with the usage of the solution mapping scheme.
- The framework implements multi-level parallelization of the material response – decomposition of the finite element domain using MPI and parallelization of the material response using OPENMP threads – resulting in reduced simulation times.
- Acceleration techniques are made use of in the computational framework to keep simulation times to a minimum. We interrogate the polycrystal model only when certain criteria are met; else a linear stress update using the elastic self-consistent moduli is performed.

To the best of our knowledge, the proposed *solution mapping scheme* and *multi-level parallelization* is entirely new and has hitherto not been presented in the literature. We have demonstrated the computational framework by simulating a two-pass ARB process. The results clearly show a through thickness gradient of texture and evolving anisotropy, which is a direct consequence of the stacking of sheets.

The current computational framework can serve as an important tool that facilitates the incorporation of the ARB process in industry – the framework incorporates a robust and reliable material model, and the two-level parallelization helps realize simulations in realistic time schedules.

Finally, we point out that the *current framework is not limited to the ARB process. It can be used for the simulation of other forming processes, including conventional rolling, deep drawing etc.*

Acknowledgments

The authors would like to thank Dr. Ingo Schmidt, Fraunhofer IWM, Freiburg, and Prof. Javier Segurado, IMDEA, Madrid, Spain for

fruitful discussions. HWH and EB would also like to gratefully acknowledge the funding of the German Research Foundation (DFG), which, within the framework of its *Excellence Initiative* supports the Cluster of Excellence *Engineering of Advanced Materials* at the University of Erlangen-Nürnberg.

References

- [1] N.R.C. Committee on Integrated Computational Materials Engineering, Integrated Computational Materials Engineering: A Transformational Discipline for Improved Competitiveness and National Security, The National Academies Press, Washington, D.C., 2008.
- [2] Y. Saito, N. Tsuji, H. Utsunomiya, T. Sakai, R. Hong, *Scr. Mater.* 39 (1998) 1221–1227.
- [3] N. Tsuji, Nanostructured metals and alloys, Woodhead Publishing, Philadelphia, 2011, pp. 40–57 (Chapter 2: Bulk Nanostructured Metals and Alloys Produced by Accumulative Roll-Bonding).
- [4] M. Ruppert, W. Böhm, H. Nguyen, H.W. Höppel, M. Merklein, M. Göken, *J. Mater. Sci.* 48 (2013) 8377–8385.
- [5] M. Göken, H.W. Höppel, *Adv. Mater.* 23 (2011) 2663–2668.
- [6] T. Hausöll, V. Maier, C.W. Schmidt, M. Winkler, H.W. Höppel, M. Göken, *Adv. Eng. Mater.* 12 (2010) 740–746.
- [7] S. Roy, B.R. Nataraj, S. Suwas, S. Kumar, K. Chattopadhyay, *J. Mater. Sci.* 47 (2012) 6402–6419.
- [8] T. Hausöll, H.W. Höppel, M. Göken, *J. Mater. Sci.* 45 (2010) 4733–4738.
- [9] C.W. Schmidt, P. Knödler, H.W. Höppel, M. Göken, *Metals* 1 (1) (2011) 65–78. <http://dx.doi.org/10.3390/met1010065>.
- [10] C.W. Schmidt, M. Ruppert, H.W. Höppel, F. Nachtrab, A. Dietrich, R. Hanke, M. Göken, *Adv. Eng. Mater.* 14 (2012) 1009–1017.
- [11] R. Jamaati, M.R. Toroghinejad, *Mater. Sci. Eng. A* 527 (27) (2010) 7430–7435.
- [12] R. Jamaati, M.R. Toroghinejad, *Mater. Sci. Eng. A* 527 (16) (2010) 4146–4151.
- [13] M. Alizadeh, M.H. Paydar, *J. Alloys Compd.* 492 (2010) 231–235.
- [14] N. Tsuji, Y. Saito, H. Lee, Y. Minamino, *Adv. Eng. Mater.* 5 (2003) 338–344.
- [15] H. Höppel, J. May, M. Göken, *Adv. Eng. Mater.* 6 (2004) 781–784.
- [16] R.Z. Valiev, I.V. Alexandrov, Y.T. Zhu, T.C. Lowe, *J. Mater. Res.* 17 (2002) 5–8. <http://dx.doi.org/10.1557/JMR.2002.0002>.
- [17] B. Beausir, J. Scharnweber, J. Jaschinski, H.-G. Brokmeier, C.-G. Oertel, W. Skrotzki, *Mater. Sci. Eng. A* 527 (2010) 3271–3278.
- [18] X. Huang, N. Tsuji, N. Hansen, Y. Minamino, *Mater. Sci. Eng. A* 340 (2003) 265–271.
- [19] C. Heason, P. Prangnell, *Mater. Sci. Forum* 408–412 (2002) 733–738.
- [20] G.I. Taylor, *J. Inst. Metals* 62 (1938) 307–327.
- [21] H. Pirgazi, A. Akbarzadeh, R. Petrov, J. Sidor, L. Kestens, *Mater. Sci. Eng. A* 492 (2008) 110–117.
- [22] P. Van Houtte, A.K. Kanjrala, A.V. Bael, M. Seefeldt, L. Delannay, *Eur. J. Mech. A/Solids* 25 (2006) 634–648.
- [23] S. Li, F. Sun, H. Li, *Acta Mater.* 58 (2010) 1317–1331.
- [24] T. Inoue, N. Tsuji, *Comput. Mater. Sci.* 46 (2009) 261–266.
- [25] F. Roters, P. Eisenlohr, L. Hantcherli, D. Tjahjanto, T. Bieler, D. Raabe, *Acta Mater.* 58 (2010) 1152–1211.
- [26] A. Prakash, Computational micromechanics of polycrystals: Special emphasis on twinning and recrystallization in Mg alloys and TWIP steels (Ph.D. thesis), Karlsruhe Institute of Technology, 2010.
- [27] F. Barbe, L. Decker, D. Jeulin, G. Cailletaud, *Int. J. Plast.* 17 (2001) 513–536.
- [28] O. Diard, S. Leclercq, G. Rousselier, G. Cailletaud, *Int. J. Plast.* 21 (2005) 691–722.
- [29] A. Prakash, S.M. Weygand, H. Riedel, *Comput. Mater. Sci.* 45 (2009) 744–750. <http://dx.doi.org/10.1016/j.commatsci.2008.06.015>.
- [30] D. Raabe, M. Sachtleber, Z. Zhao, F. Roters, S. Zaehlerer, *Acta Mater.* 49 (2001) 3433–3441.
- [31] A. Bhattacharyya, E. El-Danaf, S. Kalidindi, R. Doherty, *Int. J. Plast.* 17 (2001) 861–883.
- [32] B. Klusemann, B. Svendsen, H. Vehoff, *Comput. Mater. Sci.* 52(1) (2012) 25–32, in: Proceedings of the 20th International Workshop on Computational Mechanics of Materials – [IWCM] 20. <http://dx.doi.org/http://dx.doi.org/10.1016/j.commatsci.2011.03.042>.
- [33] R.A. Lebensohn, *Acta Mater.* 49 (2001) 2723–2737.
- [34] P. Eisenlohr, M. Diehl, R. Lebensohn, F. Roters, *Int. J. Plast.* 46 (2013) 37–53.
- [35] A. Prakash, R.A. Lebensohn, *Model. Simul. Mater. Sci. Eng.* 17 (2009) 064010. <http://dx.doi.org/10.1088/0965-0393/17/6/064010>.
- [36] F. Feyel, *Comput. Methods Appl. Mech. Eng.* 183 (2003) 309–330.
- [37] P. Van Houtte, S. Yerra, A. Van Bael, *Int. J. Plast.* 25 (2009) 332–360.
- [38] W. He, S. Zhang, A. Prakash, D. Helm, *Comput. Mater. Sci.* 82 (2014) 464–475.
- [39] R. Hill, *Int. J. Mech. Sci.* 35 (1993) 19–25.
- [40] F. Barlat, J. Yoon, O. Cazacu, *Int. J. Plast.* 23 (2007) 876–896.
- [41] N. Barton, J. Knap, A. Arsenlis, R. Becker, R. Hornung, D. Jefferson, *Int. J. Plast.* 24 (2008) 242–266.
- [42] R. Lebensohn, C. Tomé, *Acta Metall. Mater.* 41 (1993) 2611–2624.
- [43] A. Prakash, T. Hochrainer, E. Reischer, H. Riedel, *Steel Res. Int.* 79 (8) (2008) 645–652. <http://dx.doi.org/10.2374/SRI08SP030-79-2008-645>.
- [44] T. Walde, H. Riedel, *Acta Mater.* 55 (2007) 867–874.
- [45] G.C. Kaschner, J.F. Bingert, C. Liu, M.L. Lovato, P.J. Maudlin, M.G. Stout, C. N. Tomé, *Acta Mater.* 49 (2001) 3097–3108.

- [46] A. Prakash, C. Schmidt, H. Riedel, R. Kawalla, Experimental and numerical investigation of the activation of pyramidal slip during deformation of cast-rolled magnesium alloy AZ31, in: Proceedings of 8th Magnesium Conference, Weimar, Germany, 2009.
- [47] S.R. Agnew, M.H. Yoo, C.N. Tomé, *Acta Mater.* 49 (2001) 4277–4289.
- [48] C.N. Tomé, P.J. Maudlin, R.A. Lebensohn, G.C. Kaschner, *Acta Mater.* 49 (2001) 3085–3096.
- [49] J. Segurado, R.A. Lebensohn, J. Llorca, C. Tomé, *Int. J. Plast.* 28 (2012) 124–140.
- [50] M. Knezevic, R.J. McCabe, R.A. Lebensohn, C.N. Tomé, C. Liu, M.L. Lovato, B. Mihaila, *J. Mech. Phys. Solids* 61 (2013) 2034–2046.
- [51] R. Chandra, L. Dagum, D. Kohr, D. Maydan, J. McDonald, R. Menon, *Parallel Programming in OpenMP*, Morgan Kaufmann Publishers, San Francisco, 2001.
- [52] J. Eshelby, *Proc. R. Soc. A* 241 (1957) 376–396.
- [53] R.J. Asaro, *J. Appl. Mech.* 50 (1983) 921–934.
- [54] R.J. Asaro, *Adv. Appl. Mech.* 23 (1983) 1–115.
- [55] J. Hutchinson, *Proc. R. Soc. A* 348 (1976) 101–127.
- [56] T. Mura, *Micromechanics of defects in solids*, Martinus Nijhoff Publishers, The Hague, The Netherlands, 1982.
- [57] A. Molinari, G. Canova, S. Ahzi, *Acta Metall.* 35 (1987) 2983–2994.
- [58] C.N. Tomé, *Model. Simul. Mater. Sci. Eng.* 7 (5) (1999) 723.
- [59] R.A. Lebensohn, C.N. Tomé, P. Ponte Castañeda, *Philos. Mag.* 87 (2007) 4287–4322.
- [60] C. Tomé, G. Canova, U. Kocks, N. Christodoulou, J. Jonas, *Acta Metall.* 32 (1984) 1637–1653.
- [61] E. Voce, *J. Inst. Metals* 74 (1948) 537–562.
- [62] F.J. Harewood, P.E. McHugh, *Comput. Mater. Sci.* 39 (2007) 481–494.
- [63] T. Walde, H. Riedel, *Solid State Phenom.* 105 (2005) 285–290.
- [64] T. Walde, *Int. J. Refract. Metals Hard Mater.* 26 (2008) 396–403.
- [65] Abaqus Inc., Abaqus/Explicit: Advanced Topics – Appendix 3: Writing a VUMAT, Workshop, 2005.
- [66] S. Mercier, A. Molinari, *Int. J. Plast.* 25 (2009) 1024–1048.
- [67] H. Wang, P. Wu, C. Tomé, Y. Huang, *J. Mech. Phys. Solids* 58 (2010) 594–612.
- [68] H.-J. Bunge, *Texture Analysis in Materials Science: Mathematical Methods*, Cuvillier Verlag, Göttingen, 1999.
- [69] K. Shoemake, Animating rotation with quaternion curves, in: SIGGRAPH'85 Proceedings of the 12th Annual Conference on Computer Graphics and Interactive Techniques, 1985, pp. 245–254.
- [70] A. Morawiec, J. Pospiech, *Textures Microstruct.* 10 (1989) 211–216.
- [71] C.N. Tomé, R.A. Lebensohn, *Manual for VPSC–version 7* (2009).
- [72] W.G. Nöhring, Towards a finite element multiscale model of the accumulative roll bonding process (Master's thesis), Friedrich-Alexander-Universität Erlangen-Nürnberg, 2013.
- [73] W.G. Nöhring, A. Prakash, E. Bitzek, in preparation.
- [74] C.N. Tomé, R.A. Lebensohn, C.T. Necker, *Metall. Mater. Trans. A* 33 (2002) 2635–2648.
- [75] F. Bachmann, R. Hielscher, H. Schaeberle, *Solid State Phenom.* 160 (2010) 63–68. <http://dx.doi.org/10.4028/www.scientific.net/SSP.160.63>.
- [76] C. Heason, P. Prangnell, *Mater. Sci. Forum* 408–412 (2002) 733–738.
- [77] S. Li, F. Sun, H. Li, *Acta Mater.* 58 (2010) 1317–1331.
- [78] H. Tresca, *Comptes Rendus Hébd. l'Acad. Sci. Paris* 59 (1864) 754–758.
- [79] R. von Mises, *Math. Phys. Klasse* 1 (1913) 582–592.
- [80] Y. Fan, Y.N. Osetskiy, S. Yip, B. Yildiz, *Proc. Natl. Acad. Sci.* 110(44) (2013) 17756–17761. <http://dx.doi.org/10.1073/pnas.1310036110>.
- [81] E. Bitzek, P. Gumbsch, *Mater. Sci. Eng. A* 387 (2004) 11–15.
- [82] E. Bitzek, P. Gumbsch, *Mater. Sci. Eng. A* 400 (2005) 40–44.
- [83] Y. Wei, L. Anand, J. Mech. Phys. Solids 52 (11) (2004) 2587–2616. <http://dx.doi.org/10.1016/j.jmps.2004.04.006>.
- [84] D. Gianola, S.V. Petegem, M. Legros, S. Brandstetter, H.V. Swygenhoven, K. Hemker, *Acta Mater.* 54 (8) (2006) 2253–2263. <http://dx.doi.org/10.1016/j.actamat.2006.01.023>.
- [85] F. Mompiou, D. Caillard, M. Legros, *Acta Mater.* 57 (7) (2009) 2198–2209. <http://dx.doi.org/10.1016/j.actamat.2009.01.014>.
- [86] M. Meyers, D. Benson, O. Vöhringer, B. Kad, Q. Xue, H.-H. Fu, *Mater. Sci. Eng. A* 322 (12) (2002) 194–216. [http://dx.doi.org/10.1016/S0921-5093\(01\)01131-5](http://dx.doi.org/10.1016/S0921-5093(01)01131-5).
- [87] R.A. Austin, D.L. McDowell, *Int. J. Plast.* 27 (1) (2011) 1–24. <http://dx.doi.org/10.1016/j.ijplas.2010.03.002>.
- [88] H. Lim, L. Hale, J. Zimmerman, C. Battaile, C. Weinberger, *Int. J. Plast.* (2015), <http://dx.doi.org/10.1016/j.ijplas.2014.12.005> (in press).
- [89] H. Wang, P. Wu, C. Tomé, J. Wang, *Mater. Sci. Eng. A* 555 (0) (2012) 93–98. <http://dx.doi.org/10.1016/j.msea.2012.06.038>.
- [90] I. Beyerlein, R. Lebensohn, C. Tomé, *Mater. Sci. Eng. A* 345 (2003) 122–138.